Commun Nonlinear Sci Numer Simulat 82 (2020) 105069

Contents lists available at ScienceDirect

Commun Nonlinear Sci Numer Simulat

journal homepage: www.elsevier.com/locate/cnsns

Research paper

Harmonic analysis and experimental validation of bistable vibration energy harvesters interfaced with rectifying electrical circuits

Chunlin Zhang[a,b,*], R.L. Harne[c], Bing Li[d], K.W. Wang[b]

[a] School of Aeronautics, Northwestern Polytechnical University, Xi'an, Shaanxi, 710072, PR China
[b] Department of Mechanical Engineering, University of Michigan, Ann Arbor, MI 48105, USA
[c] Department of Mechanical and Aerospace Engineering, The Ohio State University, Columbus, OH 43210, USA
[d] State Key Laboratory for Manufacturing and Systems Engineering, Xi'an Jiaotong University, Xi'an, Shaanxi, 710049, PR China

ARTICLE INFO

Article history:
Received 26 September 2018
Revised 6 September 2019
Accepted 20 October 2019
Available online 21 October 2019

Keywords:
Vibration energy harvesting
Bistable oscillator
Standard rectifying electrical circuit
Performance characterization

ABSTRACT

The high-performing, nonlinear vibration energy harvesters are conventionally investigated when integrated with simplified resistive electrical circuits (AC circuits), while in fact DC voltages are needed for electronics and rechargeable batteries in practical applications. To lead to an accurate and effective set of design guidelines for realistic energy harvesting system development, an analytical, harmonic balance based method is proposed to characterize the steady state performance and investigate the DC circuit effects. During the route of the analysis method, the induced nonlinear, piecewise piezovoltage is firstly approximated via smooth dynamic responses based on the energy equivalence, which enables the followed harmonic balance operation to analytically estimate the vibration amplitude. The parameter studies show the pros and cons of the coupling constant and resistive load. In one side, with increasing the coupling constant or load resistance during their moderate range, higher electric power is extracted. In the other side, higher piezoelectric coupling and resistive load compromise the beneficial bandwidth of snap-through vibrations. Moreover, comparisons are conducted to reveal the different structural roles of the standard electrical circuit and AC circuit. It is found that AC circuit exhibits equivalent damping effect while the standard rectifying electrical circuit exhibits both equivalent damping and stiffness effects to the harvester system. These different circuit effects explain the theoretically predicted and numerically validated phenomena that the standard rectifying electrical circuit extracts less electric power than AC circuit under moderate piezoelectric coupling constants and resistive loads, while outperforms AC circuit when the coupling constants or load resistances are relatively large.

1. Introduction

The restricted life span and costly maintenance of batteries powering remote electronics or wireless sensor networks have motivated recent research efforts on converting electric power from the environmental [1,2] and human-induced [3,4] vibrations to alleviate the dependence on batteries and realize a new concept for self-powered electronics. In this domain,

* Corresponding author at: Department of Control and Information Engineering, 127 West Youyi Road, Xi'an, Shaanxi 710072, PR China.
E-mail address: zchunlin@nwpu.edu.cn (C. Zhang).

https://doi.org/10.1016/j.cnsns.2019.105069
1007-5704/

piezoelectric based electromechanical devices [5–7] have drawn much attention due to their high energy conversion efficiency [8] and easy integration into systems [9,10].

For piezoelectric energy harvesters, a mechanical oscillator is often attached to the vibration source to apply a driving stress on the coupled piezoelectric elements, and the vibration-induced voltage is further stored or consumed by a circuit interface [11]. To date, many researches have focused on broadening the beneficial bandwidth of piezoelectric harvesters to satisfy broadband base excitations [12–14]. Bistable harvesters, that possess two configurations of static equilibrium, have gained particular attention since the snap-through effect of oscillating from one stable state to another can generate high power output [15–17]. Numerous bistable harvester configurations have been designed, including the buckled beam bridge [18–21], cantilevered beam with repulsive [22–24] or attractive magnet forces [25,26], and cantilevered bistable plate [27]. The dynamic behaviors and energy harvesting performance of bistable structures have been investigated via numerical methods [28,29], analytical analysis [30,31] including harmonic balance analysis [32,26], and experimental validations [33]. Collectively, the findings have revealed that snap-through may be activated regardless of the form or frequency of input excitation, making bistable harvesters potentially more beneficial in realistic environments. However, most of these studies consider that the piezoelectric element is directly connected with an electrical load resistance, thus only a simplified AC power is considered [9]. Yet, in practice most electronic devices or rechargeable batteries require a DC voltage, such that the electric circuit that interfaces the piezoelectric element and terminal electronics must rectify the AC power to DC power [34].

There are several nonlinear circuits considered to rectify the AC voltage or further enhance the conversion ability of piezoelectric elements [35–37], including the standard diode bridge-based circuit [38,39], synchronized switch harvesting on inductor (SSHI) [40–42], tunable parallel synchronized switch harvesting on inductance (PSSHI) [43], the synchronous electric charge extraction (SECE) circuits [44,45], short-circuit synchronous electric charge extraction (SC-SECE) [46], and frequency tuning synchronous electric charge extraction (FT-SECE) [47]. However, such energy capture and storage circuit performances are typically estimated or optimized when connected to a linear energy harvester. Only a few studies have characterized the performance of bistable harvesters interfaced with rectifying electrical circuits. Chen et al. compared the harvested power of bistable harvester interfaced with switching and standard circuits using a work-cycle method [48]. Liu et al. studied the bistable harvester coupled with optimized SECE circuit [49]. Singh et al. investigated the performance obtained by connection to the SCE (synchronous charge extraction) circuit [50]. Wu proposed synchronous mechanical switches to passively rectify the induced voltage into DC form [51]. Cheng et al. proposed COV-PSSHI circuit to enhance the energy harvesting performance [52]. Dai et al. investigated the DC power extraction performance under combined harmonic and stochastic excitations [53]. Lan et al. proposed a numerical, Newton's method enabled harmonic balance technique to analyze the performance of the monostable energy harvester interfaced with the standard rectifying electrical circuit [54]. Considering the induced piezovoltage from the DC circuits exhibits piecewise property due to the alternative conducts and blocks of the rectifying diode bridge, the standard harmonic balance method could not be directly used to estimate the dynamic responses. Thus, these investigations surveyed above mainly focus on studies using numerical simulation methods complemented by experimental investigations. There remains the need for a more rigorous and analytical characterization of the system performance resulting from the interaction of bistable harvesters and nonlinear circuits.

The goal of this research is to advance the state of the art and comprehensively investigate the performance of bistable harvesters interfaced with the rectifying electrical circuit. Here we will focus our study on utilizing a standard type of rectifying circuit, in which a rectifier bridge followed by a capacitor is used to rectify the piezovoltage from AC to DC power. This circuit composition continues to attract attention because it operates passively, and as such does not need external control or energy input. To achieve the research goal, an analytical approach is proposed to provide a rigorous and systematic framework for insightful analysis. Through the combination of analytical, numerical, and experimental efforts, this research uncovers the influences of the coupling between the nonlinear bistable vibration energy harvester and the nonlinear standard rectifying electrical circuit to store electric power converted from the input excitation. The investigation also illustrates the different effects of the standard rectifying electrical circuit and AC circuit on the system dynamics and energy harvesting performance.

The rest of this paper is organized as follows. The bistable harvester system coupled with the standard rectifying electrical circuit and its governing equations are reviewed in Section 2. The mathematical formulation and procedures undertaken to analytically predict the steady state dynamics and harvested power under harmonic excitation are presented in Section 3. Section 4 discusses the experimental system setup. In Section 5, the system performance is characterized under different excitation levels and frequencies, and the role of the interfaced circuit is explored. Finally, the performance of the interfaced system with respect to excitation level and frequency, and circuit parameters is validated via experiments, as discussed in Section 6.

2. System model

Bistable energy harvesters are implemented widely using a cantilever with repulsive or attractive magnet pairs on the free end, or a buckled beam under axial compressive force mechanisms [9,55]. In such architectures, it is well established that the nonlinear stiffnesses are approximated via negative linear and positive cubic components in a restoring force expansion [9]. For a general understanding of the mechanism of such bistable energy harvesting systems, in this study, the harvester of interest is generalized as a base-excited bistable oscillator having piezoelectric conversion mechanism, and the

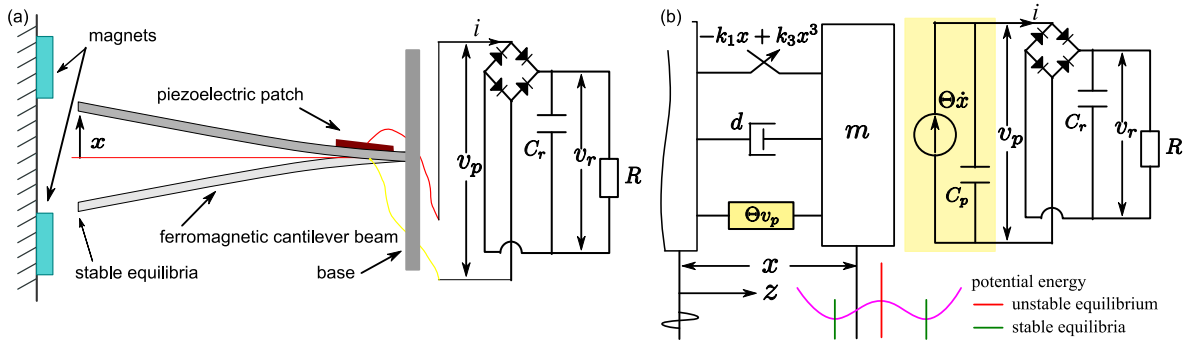

Fig. 1. Bistable energy harvester interfaced with standard rectifying electrical circuit: (a) prototypical bistable, piezoelectric energy harvester; and (b) equivalent model for the dynamic system.

latter component is interfaced with an external standard rectifying electrical circuit which converts the piezovoltage from AC to DC form. Fig. 1(a) illustrates a typical prototype of bistable, piezoelectric harvester interfaced with the standard rectifying circuit. The bistable system is equivalized as a lumped-parameter model by strict mathematic derivation [56], as shown in Fig. 1(b). The governing equation for the coupled system are expressed as:

$$m\ddot{x}+d\dot{x}-k_1x+k_3x^3+\Theta v_p=-m\ddot{z} \tag{1}$$

$$\Theta\dot{x}-C_p\dot{v}_p=i \tag{2}$$

$$i=\begin{cases} C_r\dot{v}_r+v_r/R, & \text{if } v_p=v_r \\ -C_r\dot{v}_r-v_r/R, & \text{if } v_p=-v_r \\ 0, & \text{if } |v_p|<v_r \end{cases} \tag{3}$$

where x is the relative displacement of the effective mass m with respect to base; z is the base motion given by $\ddot{z}=-p\cos\omega t$ where p and ω are the amplitude and frequency of the base oscillation, respectively; d is the viscous damping constant; k_1 and k_3 are the linear and nonlinear stiffnesses, respectively; Θ is the force-voltage coupling factor; v_p is the voltage across the piezoelectric capacitance C_p; i is the current flow through the diode bridge which rectifies the piezovoltage into DC voltage; v_r is the voltage across the filter capacitance C_r in parallel with the load resistance R. Under harmonic excitation, the structure may exhibit high-orbit snap-through vibration around the three equilibrium points including two stable equilibria $x^*=\pm\sqrt{k_1/k_3}$ and one unstable equilibrium $x^*=0$, or low-orbit intrawell vibration which oscillates around only one of the stable equilibrium positions. These two dynamic regimes result in dramatically different effectiveness in energy conversion in the vibration energy harvesting context.

3. Analytical estimation using harmonic balance based method

In the routine of the proposed analytical method, a prior processing is conducted to approximate the piecewise piezovoltage via the smooth dynamic responses based on the energy equivalence, which enables the further adoption of harmonic balance analysis to estimate the vibration amplitude. The steady state dynamic responses of bistable structures under harmonic excitation usually contain the fundamental motion which shares the same oscillating frequency with the excitation force and the higher harmonic components. Considering the fundamental frequency component plays a crucial role in the vibration responses on a wide range of excitation frequencies, only the fundamental frequency component is considered in this analysis. Accordingly, the vibration displacement can be assumed as

$$x=a\cos\omega t+b\sin\omega t+c=A\cos(\omega t-\psi)+c \tag{4}$$

where a, b and c vary slowly in time for steady state dynamic responses; $A=\sqrt{a^2+b^2}$ and ψ are displacement amplitude and phase lag, respectively; $a=A\cos\psi$; $b=A\sin\psi$; c describes the displacement offset of the bistable device since the oscillator permits oscillations around either of the stable equilibrium positions, while c is 0 for snap-through vibration which denotes large amplitude displacements that span the two stable equilibria positions.

3.1. Smooth representation of the piecewise piezovoltage

The standard rectifying electrical circuit is interfaced with the periodically strained piezoelectric elements of the bistable harvester to obtain smooth DC voltage outputs. Here the diode is assumed to be perfect such that no voltage-drop occurs when the current flows through. The output DC voltage v_r must be stabilized in most applications, and a feasible approach

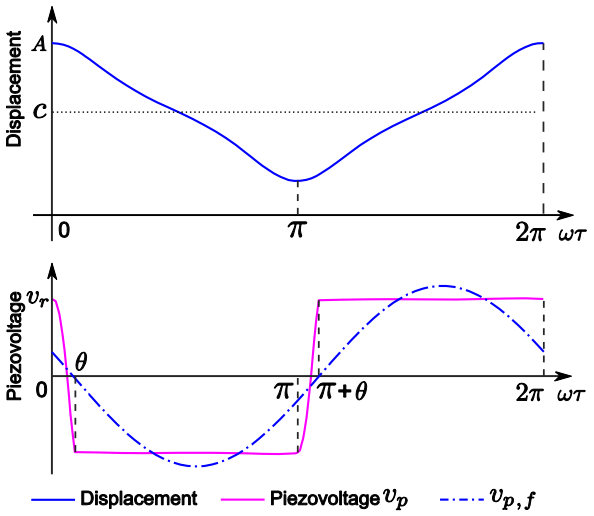

Fig. 2. Typical piezovoltage and its fundamental harmonic component.

to achieve this is to adopt a relatively large filtering capacitance C_r so that v_r is near constant over the course of an excitation period.

A new variable $\omega\tau = \omega t - \psi$ is introduced. The displacement is expressed as $x = A\cos\omega\tau + c$, which starts from its maximum point when $\tau(0) = 0$. As illustrated in Fig. 2, the rectifier bridge alternatively conducts and blocks the current flow during one base excitation cycle. When the absolute value of the piezovoltage $|v_p|$ reaches the rectified voltage v_r, the bridge conducts and the current flows into the circuit. On the other hand, the bridge remains blocked during the interval when $|v_p| < v_r$. The state switching of the rectifier bridge from being conducted to being blocked occurs at the maxima points of the vibration displacement which are also the zero-crossing points of the velocity. The piezovoltage v_p is piecewise due to the alternating state of current provided at the diode bridge output. Based on the assumption that near constant rectified DC voltage is obtained in this research via adopting a relatively large filtering capacitance in the system, the piezovoltage is derived using Eqs. (2), (3) and (4).

$$v_p = \begin{cases} \dfrac{\Theta A}{C_p}(\cos(\omega\tau) - 1) + v_r, & \omega\tau \in [0, \theta); \\ -v_r, & \omega\tau \in [\theta, \pi); \\ \dfrac{\Theta A}{C_p}(\cos(\omega\tau) + 1) - v_r, & \omega\tau \in [\pi, \pi + \theta); \\ v_r, & \omega\tau \in [\pi + \theta, 2\pi]. \end{cases} \tag{5}$$

where θ is the rectifier blocked angle in half an oscillation cycle and satisfies

$$\frac{\Theta A}{C_p}(\cos\theta - 1) + v_r = -v_r. \tag{6}$$

Considering that the averaged charge flow through the rectifier bridge equals that consumed on the load resistance during one base motion cycle, the integration of Eq. (2) on half the vibration period $0 \le \omega\tau \le \pi$ equals that of Eq. (3).

$$\int_0^{\pi} (\Theta\dot{x} - C_p\dot{v}_p)d\omega\tau = -2\Theta A + 2C_p v_r = \int_0^{\pi} (-C_r\dot{v}_r - v_r/R)d\omega\tau \approx -\frac{v_r}{R}\cdot\frac{\pi}{\omega}. \tag{7}$$

Combining Eqs. (6) and (7), one obtains

$$v_r = \frac{\Theta A R\omega}{\omega C_p R + \pi/2}; \tag{8}$$

$$\cos\theta = 1 - \frac{2C_p R\omega}{\omega C_p R + \pi/2}. \tag{9}$$

The piecewise piezovoltage v_p is then approximated using its fundamental harmonic component $v_{p,f}$. This is a strategy proposed by Liang and Liao [39] based on the energy balance thought [38] in the analysis of linear harvesting systems. Considering v_p is a periodic function with period $T = 2\pi/\omega$, its fundamental harmonic component is obtained via expanding

v_p in Fourier series

$$\begin{aligned} v_{p,f} &= \frac{\Theta A}{2\pi C_p}\left[(2\theta - \sin 2\theta)\cos\omega\tau - 2\sin^2\theta \sin\omega\tau\right] \\ &= \frac{\Theta}{2\pi C_p}\left\{\left[a(2\theta - \sin 2\theta) + b\cdot 2\sin^2\theta\right]\cos\omega t + \left[-a\cdot 2\sin^2\theta + b(2\theta - \sin 2\theta)\right]\sin\omega t\right\} \end{aligned} . \tag{10}$$

During one vibration cycle, the waveforms of typical piezovoltage and its smooth representation are illustrated in Fig. 2. From the waveform point of view, deviation is observed between v_p and its fundamental harmonic component $v_{p,f}$. While from the power point of view, the averaged energy extracted via piezoelectric element during one vibration cycle is expressed as

$$E_{pzt} = \frac{1}{T}\int_0^T \Theta v_p \dot{x} dt. \tag{11}$$

Considering that $\dot{x}$ is orthogonal to the high-order harmonics of v_p and their inner products will be null based on the assumed forms of the displacement and velocity functions, thus representing v_p with $v_{p,f}$ is reasonable for energy estimation of the harvester system.

3.2. Estimation of vibration amplitude and harvested power

Substituting Eq. (4) and its first- and second-order derivatives as well as Eq. (10) into the governing Eq. (1), the coefficients of the constant, $\sin\omega t$ and $\cos\omega t$ are separately equated based on the harmonic balance method

$$d\dot{c} = -c\left[-k_1 + \frac{3}{2}k_3\left(a^2 + b^2\right) + k_3c^2\right]; \tag{12}$$

$$d\dot{a} + 2m\omega\dot{b} = ak_1 - \frac{3}{4}k_3a\left(a^2 + b^2\right) - 3k_3ac^2 - bd\omega + ma\omega^2 - \frac{a\Theta^2}{2\pi C_p}(2\theta - \sin 2\theta) - \frac{b\Theta^2}{\pi C_p}\sin^2\theta + mp \tag{13}$$

$$-2m\omega\dot{a} + d\dot{b} = bk_1 - \frac{3}{4}k_3b\left(a^2 + b^2\right) - 3k_3bc^2 + ad\omega + mb\omega^2 + \frac{a\Theta^2}{\pi C_p}\sin^2\theta - \frac{b\Theta^2}{2\pi C_p}(2\theta - \sin 2\theta). \tag{14}$$

Steady state dynamics are predicted in the event that the time derivatives are zero. Using this assumption, a and b can be expressed using the external force and vibration amplitude$A$.

$$a = \frac{mp\left[-k_1 + 3k_3A^2/4 + 3k_3c^2 - m\omega^2 + \Theta^2(2\theta - \sin 2\theta)/2\pi C_p\right]}{\left[-k_1 + 3k_3A^2/4 + 3k_3c^2 - m\omega^2 + \Theta^2(2\theta - \sin 2\theta)/2\pi C_p\right]^2 + \left[d\omega + \Theta^2\sin^2\theta/\pi C_p\right]^2}; \tag{15}$$

$$b = \frac{mp\left[d\omega + \Theta^2\sin^2\theta/\pi C_p\right]}{\left[-k_1 + 3k_3A^2/4 + 3k_3c^2 - m\omega^2 + \Theta^2(2\theta - \sin 2\theta)/2\pi C_p\right]^2 + \left[d\omega + \Theta^2\sin^2\theta/\pi C_p\right]^2}. \tag{16}$$

The vibration amplitude A can then be estimated based on the relationship$A^2 = a^2 + b^2$. For snap-through motion oscillating symmetrically around the three equilibrium points, the variables are calculated to satisfy

$$c = 0; \tag{17}$$

$$A^2\left\{\left[\frac{3}{4}k_3A^2 - m\omega^2 - k_1 + \frac{\Theta^2}{2\pi C_p}(2\theta - \sin 2\theta)\right]^2 + \left[d\omega + \frac{\Theta^2}{\pi C_p}\sin^2\theta\right]^2\right\} - (mp)^2 = 0. \tag{18}$$

On the other hand, for intrawell oscillation, the nonzero constant c and vibration amplitude can be calculated to meet

$$c^2 = \frac{k_1}{k_3} - \frac{3}{2}A^2; \tag{19}$$

$$A^2\left\{\left[-\frac{15}{4}k_3A^2 - m\omega^2 + 2k_1 + \frac{\Theta^2}{2\pi C_p}(2\theta - \sin 2\theta)\right]^2 + \left[d\omega + \frac{\Theta^2}{\pi C_p}\sin^2\theta\right]^2\right\} - (mp)^2 = 0. \tag{20}$$

Thus the displacement amplitudes of snap-through and intrawell vibrations can be obtained via solving the roots of Eqs. (18) and (20), respectively. These amplitude expressions are derived via the harmonic balance method, and similar derivations could be found in analyzing the harmonic responses of the bistable oscillator [16] or the bistable energy harvester interfaced with an AC circuit [32]. Eqs. (18) and (20) are one variable cubic equations with the variable $A^2$and may be directly solved via the Cardano formula or via straightforward root evaluation algorithms. The latter approach is employed in this research using the *roots* command in the MATLAB software.

Considering the harvested power is consumed by the load resistance, the harvested power can be estimated and expressed as a function of the vibration amplitude from Eq. (8).

$$P = \frac{v_r^2}{R} = \frac{\Theta^2 A^2 \omega^2 R}{(\omega C_p R + \pi/2)^2}. \tag{21}$$

3.3. Stability analysis of the analytical results

Though separately six roots satisfy the governing Eqs. (18) and (20) of the vibration amplitude in the snap-through and intrawell regimes, respectively, only a few physical meaningful solutions can be realized in practice. A stability evaluation is performed to identify the stable responses that are physically meaningful and can be realized experimentally. Eqs. (12)–(14) are cast into the form $\mathbf{L}\cdot\dot{\vec{y}} = \mathbf{F}(\vec{y})$, where vector $\vec{y}$ is defined as $\vec{y} = [c,\ a,\ b]^T$. The matrix $\mathbf{L}$ and vector $\mathbf{F}$ are thus expressed as:

$$\mathbf{L} = \begin{bmatrix} d & 0 & 0 \\ 0 & -2m\omega & d \\ 0 & d & 2m\omega \end{bmatrix} \tag{22}$$

$$\mathbf{F}(\vec{y}) = \begin{bmatrix} -c\left[-k_1 + \frac{3}{2}k_3\left(a^2+b^2\right) + k_3c^2\right] \\ ak_1 - \frac{3}{4}k_3a\left(a^2+b^2\right) - 3k_3ac^2 - bd\omega + ma\omega^2 - \frac{a\Theta^2}{2\pi C_p}(2\theta - \sin 2\theta) - \frac{b\Theta^2}{\pi C_p}\sin^2\theta + mp \\ bk_1 - \frac{3}{4}k_3b\left(a^2+b^2\right) - 3k_3bc^2 + ad\omega + mb\omega^2 + \frac{a\Theta^2}{\pi C_p}\sin^2\theta - \frac{b\Theta^2}{2\pi C_p}(2\theta - \sin 2\theta) \end{bmatrix} \tag{23}$$

Stability of steady state dynamic predictions may be determined by assessing the eigenvalues of the Jacobian of $\mathbf{G} = \mathbf{L}^{-1}\cdot\mathbf{F}(\vec{y})|_{\vec{y}=\vec{y}_0}$ where $\vec{y}_0$ represents the steady state responses from the aforementioned analysis. The dynamic response is determined to be stable only if all the eigenvalues' real parts are negative. It is noted that the external disturbance is not considered in this research, and the stable solutions indicate physically reachable vibrations and couldn't reveal the vibrations stability or robustness under external disturbance [57].

4. Experimental system setup

The parameters used throughout the following analytical and numerical studies correspond to the experimental system utilized in this research. The main mechanical structure is a bistable cantilever beam with piezoelectric transducer patches, as shown in Fig. 3.

The spring steel cantilever of length 133.35 mm, width 12.7 mm and thickness 0.508 mm is ferromagnetic and mounted in the horizontal orientation such that gravitational influence does not affect the beam transverse response. Two impulsive magnets are spaced approximately $\delta = 7.14$ mm away from the cantilever tip, and the center-to-center distance of the two magnets is $\Delta = 26.98$ mm. Thus, the bistability is induced due to the combination of elastic and magnetic forces exerted at the beam tip, and the primary generalized displacement is the beam tip motion. In this configuration, the two intrawell

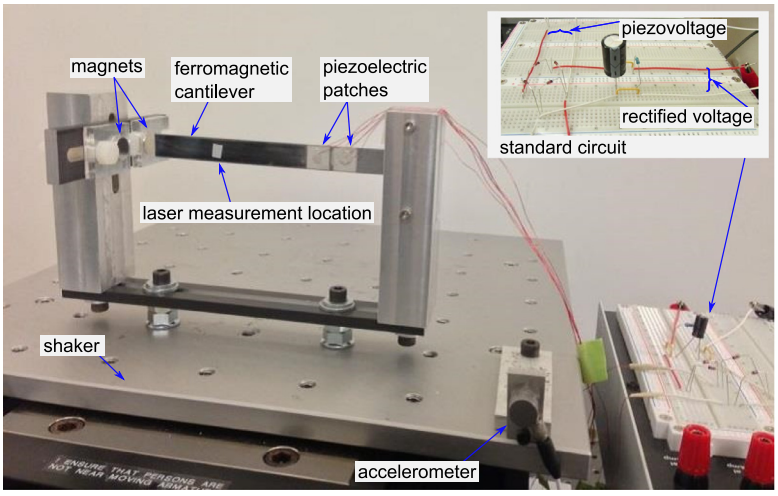

Fig. 3. Experiment systems.

Table 1
Parameters of the experimental setup.

Component	Value or model
mass, m [g]	1.92
damping, d [N.s/m]	3.92×10^{-3}
stiffness, k_1 [N/m]	23.2
stiffness, k_3 [N/m^3]	5.37×10^5
piezoelectric coupling, Θ [N/V]	0.0327×10^{-3}
piezo capacitance, C_p [F]	1.28×10^{-8}
filter capacitance, C_r [F]	4.7×10^{-5}
resistance, R [kΩ]	56

natural frequencies were measured to be 25.06 Hz and 24.44 Hz with stable equilibria at $\bar{x} = \pm 6.57$ mm, ensuring as close to ideal symmetry of the double-well potential was achieved. On each side of the beam, two piezoelectric patches of length 11.1 mm and width 12.7 mm are bonded to the beam surface in series using silver epoxy (MG Chemicals 8831) such that the patch centers are spaced from the cantilevered end by 22.2 mm and 37.3 mm, respectively. In the experiments hereafter, only two piezoelectric elements bonded to one side of the beam (see Fig. 3) are connected through the circuit [40], and the total capacitance is measured to be $C_p = 1.28 \times 10^{-8}$F. The piezoelectric elements are then interfaced with a standard diode bridge-based rectifying electrical circuit in which the filter capacitance and load resistance are chosen as $C_r = 47\mu$F and $R = 56$kΩ, respectively. The forward voltage drop of the rectifier diode is measured to be about 0.4 V. The bistable structure is mounted on an electrodynamic shaker (APS ELECTRO-SEIS) of which the base motion can be controlled. An accelerometer (PCB-352C33) is installed at the end of the shaker to track the base acceleration. Measurements of the vibration displacement and velocity of the bistable beam are also acquired using the laser interferometers (Polytec OFV-3001, OFV-5000) and of the rectified voltage across the load resistance R.

To provide comparable analysis with experiments, the effective system parameters in the lumped model with the governing Eq. (1) are estimated based on the mathematical derivatives and formulas in Ref. [58,56]. These effective system parameters are identified basically from measurements (e.g., the damping constant by the log-decrement method, and the linear stiffness from the natural frequency of the perturbation responses around the stable equilibrium, and capacitance by multi-meter readout) or effective relations (e.g., the equivalent mass of a cantilevered beam from Ref. [59], and equivalent excitation amplitude based on the accelerometer measurement with a multiplicative factor [56]) and presented in Table 1.

5. Analytical investigations

In this section, the system performances are characterized under different external excitation levels and frequencies. Considering the effects of the system geometry parameters of bistable harvesters on the dynamics have been widely investigated [60], the influence of the electromechanical coupling constant and load resistance of the DC circuit on the system performance is studied. Also, the influence of the standard rectifying electrical circuit is explored, and quantitatively and qualitatively compared with the AC circuit (pure resistive load interface) on the harvester responses. The system parameters employed are the same as those in Table 1. The linear natural frequency of the mechanical oscillator can be calculated as $\omega_n = \sqrt{k_1/m}$. A normalized frequency $\upsilon = \omega/\omega_n$ is adopted in the analysis hereafter which provides the ratio of the excitation frequency to the linear natural frequency.

5.1. Performance characterization with respect to excitation amplitude and frequency

The steady state dynamics and energy harvesting performance are characterized with different excitation amplitudes and a wide frequency range of $0 < \upsilon \leq 3$. Considering that the harvested power has the same trend as the rectified voltage for fixed load resistance, only the harvested power is displayed here. For quantitative description and comparison of the excitation level, the dimensionless excitation amplitude adopted in existing work is calculated as $\bar{p} = p/x_0\omega_n^2$ where x_0 is the static equilibrium expressed as $x_0^2 = k_1/k_3$ [26]. Additionally, the analytical predictions are compared with the numerical results calculated via a fourth-order Runge-Kutta algorithm of Eqs. (1)–(3) conducted in the software MATLAB with 15 randomly generated initial conditions. Fig. 4(a) and (b), respectively, present the amplitude of the fundamental harmonic component of vibration displacement and the harvested power for a weak excitation level of $p = 0.8$m/s^2 ($\bar{p} = 0.010$). The solid (dashed) lines are analytical estimations of the stable (unstable) responses, while the circles present numerical simulation counterparts. It reveals that under weak excitation the high-orbit snap-through vibration that spans between the two stable equilibria is always coexisted with low-orbit intrawell vibration. Comparison between analytical and numerical predictions shows good agreement in general, while in certain cases the analytical method predicts potential vibrations whereas the corresponding numerical results are not tracked in the limited attempts.

Figs. 5 and 6 show the dynamic responses and harvested powers under greater excitation levels of $p = 2.5$m/s^2 ($\bar{p} = 0.032$) and $p = 15$m/s^2 ($\bar{p} = 0.189$), respectively. The two cases marked using the triangle and diamond in Fig. 6 are illustrated in Fig. 7, with the numerically simulated dynamic responses, induced voltage and electric current. It is shown that the induced piezovoltage and electric current during one vibration cycle are divided into charging and discharging stages,

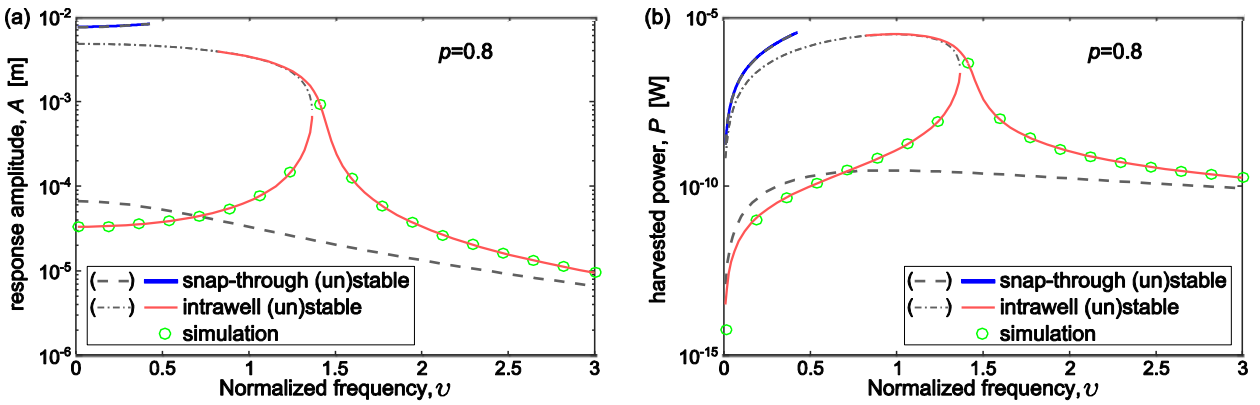

Fig. 4. Frequency dependence of (a) response amplitude and (b) harvested power for $p = 0.8\text{m/s}^2$.

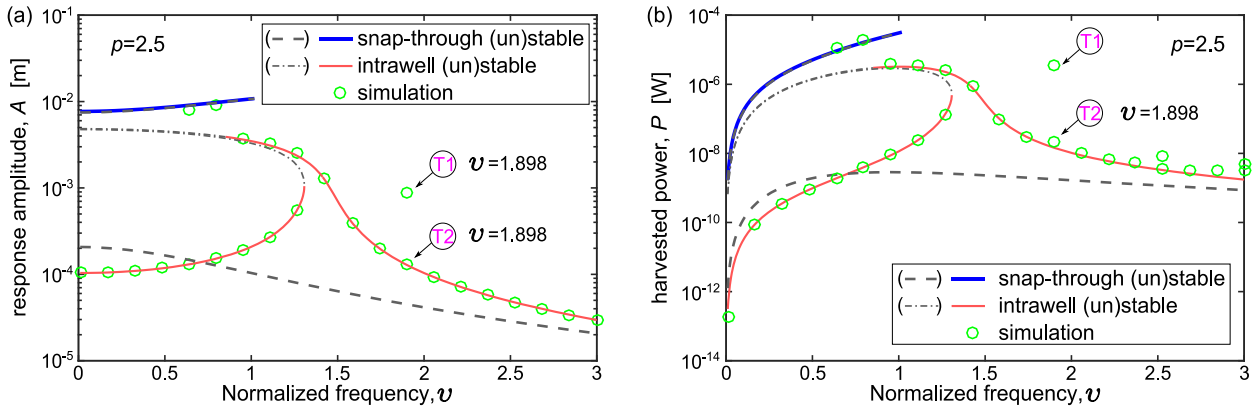

Fig. 5. Frequency dependence of (a) response amplitude and (b) harvested power for $p = 2.5\text{m/s}^2$.

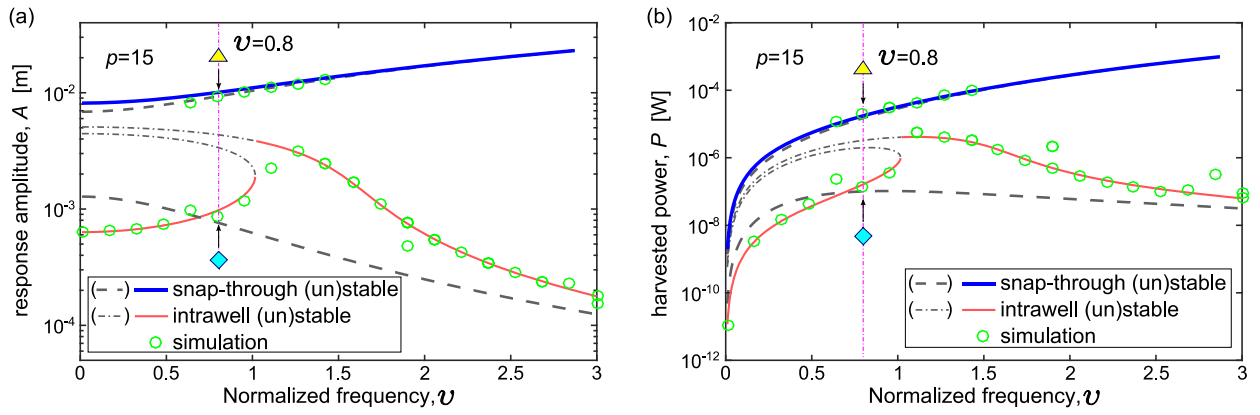

Fig. 6. Frequency dependence of (a) response amplitude and (b) harvested power for $p = 15\text{m/s}^2$. The triangle and diamond indicate the excitation frequency υ=0.8under which the time varying waveforms of the dynamic responses and induced voltages are numerically estimated and shown in Fig. 7.

and the vibration amplitude and extracted DC voltage from the snap-through vibration are much larger than those from the intrawell vibration. It also reveals that the dynamic response in Fig. 7(b) is not sinusoidal due to the existence of higher harmonics, and slight prediction error is thus produced by the analytical method in predicting the vibration amplitude and harvested DC voltage because only one-term, fundamental frequency component is considered.

From Figs. 4–6, it is concluded that when larger excitation amplitude is applied, the effective frequency range activating snap-through vibration is wider, whereas the two intrawell branches are shortened and thus a unique frequency range that only activates snap-through vibrations is presented under relatively large excitation level. In general, the results reveal that analytical predictions faithfully predict the trend of harvester responses, while finite deviation between analytical and

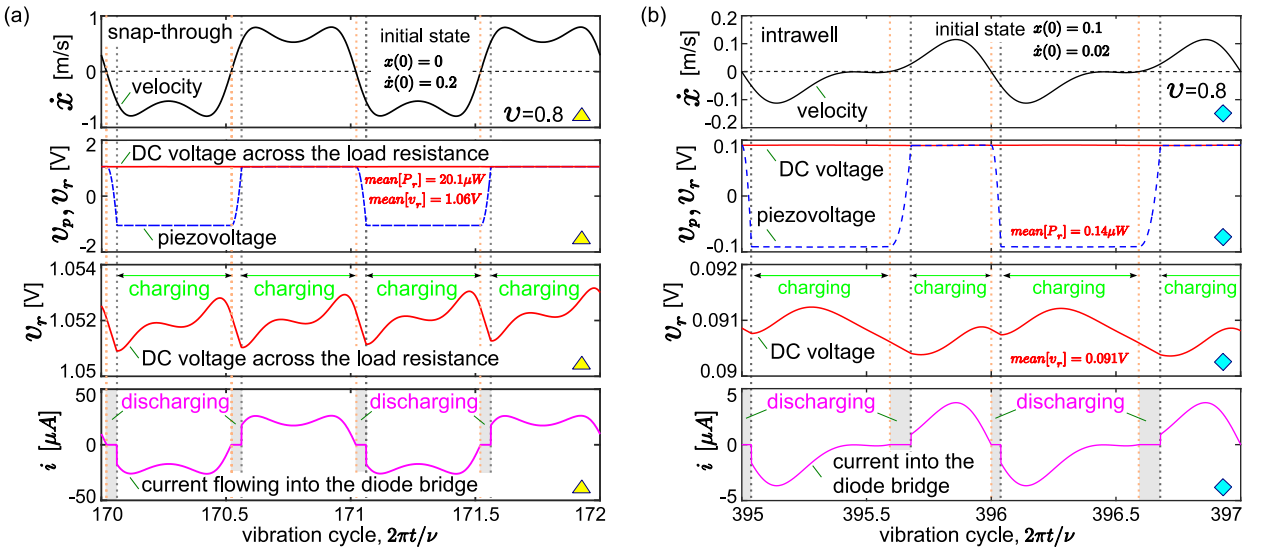

Fig. 7. Numerically simulated waveforms of the dynamic responses, induced voltages and electrical current in (a) snap-through regime and (b) intrawell regime.

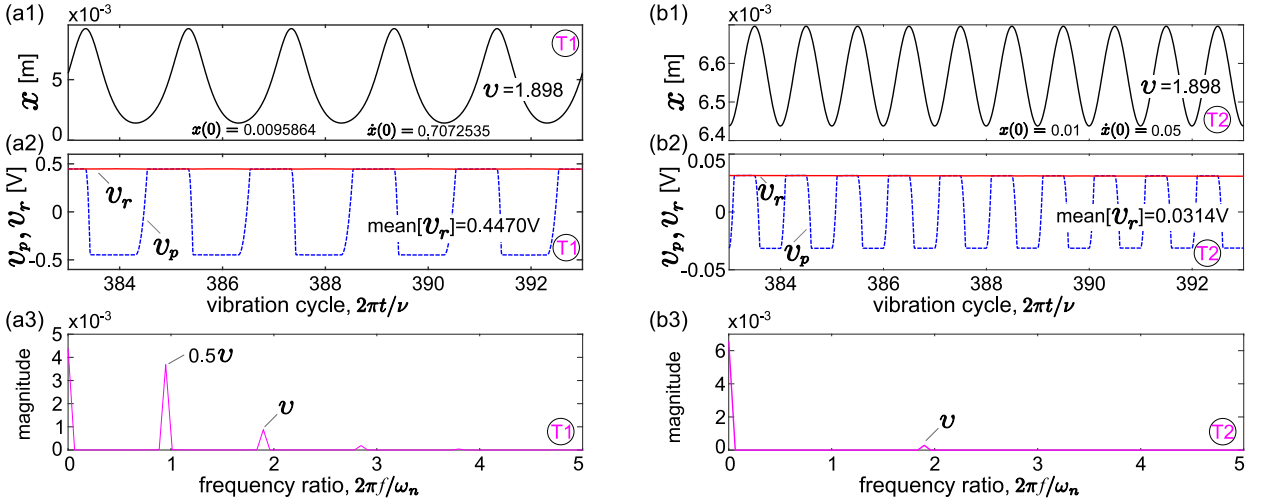

Fig. 8. Numerical results of the intrawell oscillations as indicated by the labels T1 and T2 in Fig. 6. Here, (a) is the motion labeled by T1, and (b) corresponds to the motion labeled by T2. The up-to-low rows are the displacement, induced voltage, and frequency spectrum of the displacement, respectively.

numerical results especially for relatively large excitation level is observed when the normalized excitation frequency is around 2. Fig. 8 illustrates the simulated dynamic responses and induced voltage of the intrawell oscillations as indicated by the labels T1 and T2, respectively. Besides the zero-frequency component which corresponds to the displacement drift of the intrawell oscillation, it is found the fundamental frequency component is the primary component in the Fig. 8(b3), and thus the analytical prediction is in good agreement with numerical result. However, for the subharmonic resonance vibration shown in Fig. 8(a1), the subharmonic component is primary and higher harmonic components are also observed, obvious error occurs in the analytical estimation when only one-term harmonic function is used to describe the response.

5.2. Effect of load resistance

The load resistance located in the standard rectifying electrical circuit consumes the harvested electrical power and thus has damping effect on the harvester dynamics. To investigate the influence of load resistance on the system dynamics and energy harvesting performance, three different load resistances of $R_1 = 100\Omega$, $R_2 = 10\text{k}\Omega$ and $R_3 = 1\text{M}\Omega$ are adopted to estimate the steady state vibration amplitude, rectified voltage and harvested power on the excitation frequency range of $0 < \upsilon \leq 3$ with the excitation amplitude fixed at $p = 7\text{m/s}^2$. The electromechanical coupling constant is $\Theta = 3.27 \times 10^{-3}\text{N/V}$

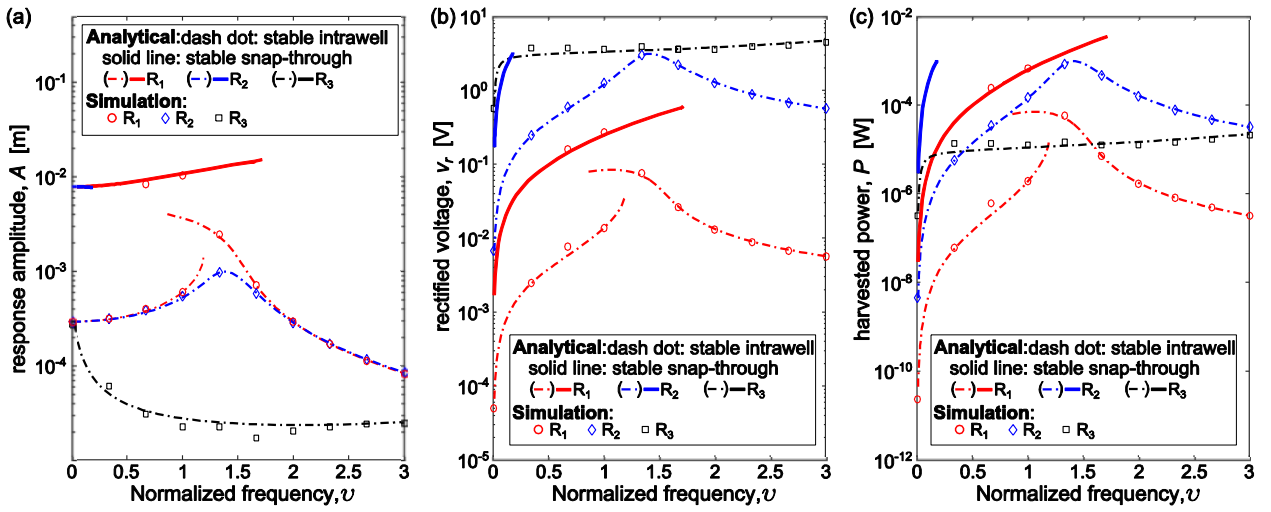

Fig. 9. Influence of load resistance on (a) dynamic response; (b) rectified voltage and (c) harvested power. The load resistances are $R_1 = 100\Omega$, $R_2 = 10\text{k}\Omega$ and $R_3 = 1\text{M}\Omega$.

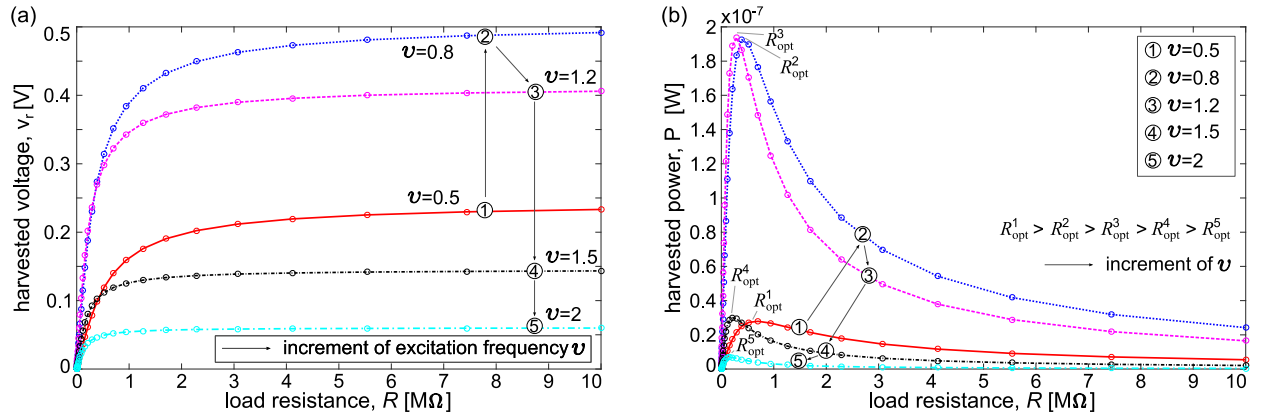

Fig. 10. Numerically estimated influence of load resistance on (a) rectified voltage and (b) harvested power of a linear vibration energy harvester interfaced with standard rectifying electric circuit.

and the other system parameters are chosen the same as those in Table 1. The analytically predicted stable responses and corresponding numerical simulation results are displayed in Fig. 9.

For a qualitative comparison, a linear harvester interfaced with the standard rectifying electric circuit is considered. The governing equation of the mechanical oscillator is $m\ddot{x} + d\dot{x} + k_1 x + \Theta v_p = mp\cos(\upsilon\omega_n t)$ and that of the circuit is the same as Eqs. (2) and (3). Adopting the same system parameters as listed in Table 1, the dynamic response and harvested power are numerically estimated under the excitation strength $p = 2.5$ and a set of excitation frequencies, and the results are shown in Fig. 10.

For a linear system, with increment of the load resistance, the rectified voltage increases in the moderate range of the load resistance and then becomes stable for relatively large load resistance; while the harvested power first increases to the maximum and then gradually decreases. Moreover, the optimal load resistance corresponding to the maximal harvested power is excitation frequency dependent and turns to be smaller for higher excitation frequency. On the other hand, the effect of the load resistance on the bistable energy harvester is more complicated. From Fig. 9(a), it is shown that greater load resistance will compromise the beneficial bandwidth of snap-through vibration. For moderate load resistance such as for$R < R_2 = 10\text{k}\Omega$, greater load resistance slightly decreases the vibration amplitude on each vibration branch; while for relatively large load resistance such as $R_3 = 1\text{M}\Omega$, the vibration amplitude is significantly attenuated and the snap-through vibration no longer occurs. Fig. 9(b) reveals that higher rectified voltages are extracted by greater load resistance in both snap-through and intrawell vibration regimes because more voltage will be distributed across the load resistance. It is noted that the contact point of the rectified voltages induced from load resistances R_2 and R_3 at frequency $\upsilon = 1.34$ in Fig. 9(b) means that the rectified voltage already reaches its maximum at this excitation frequency. Accordingly, it is concluded that in the low frequency range, the maximal harvested power under fixed excitation frequency is obtained via the maximal

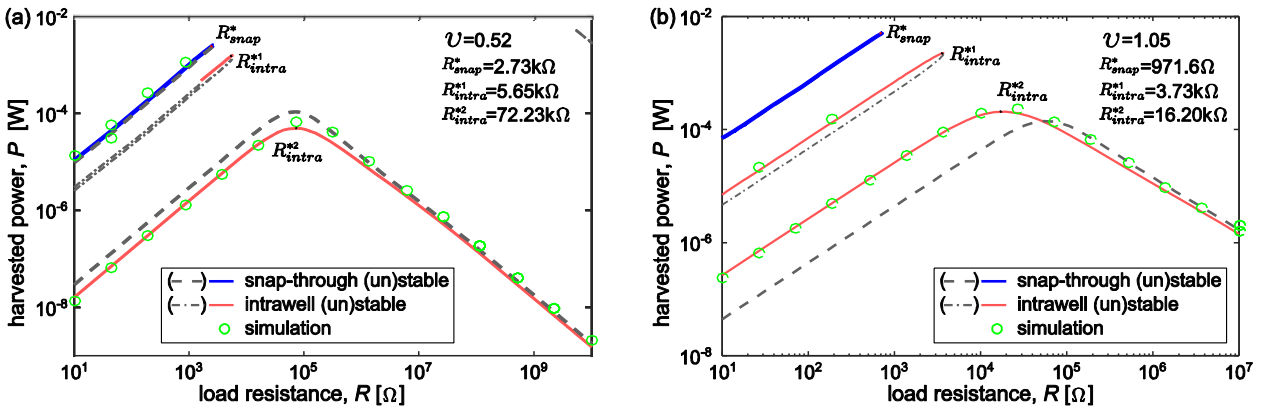

Fig. 11. Load resistance dependence of the harvested power under the excitation level of $p = 8\text{m/s}^2$, and frequencies of (a) $\upsilon = 0.52$ and (b) $\upsilon = 1.05$.

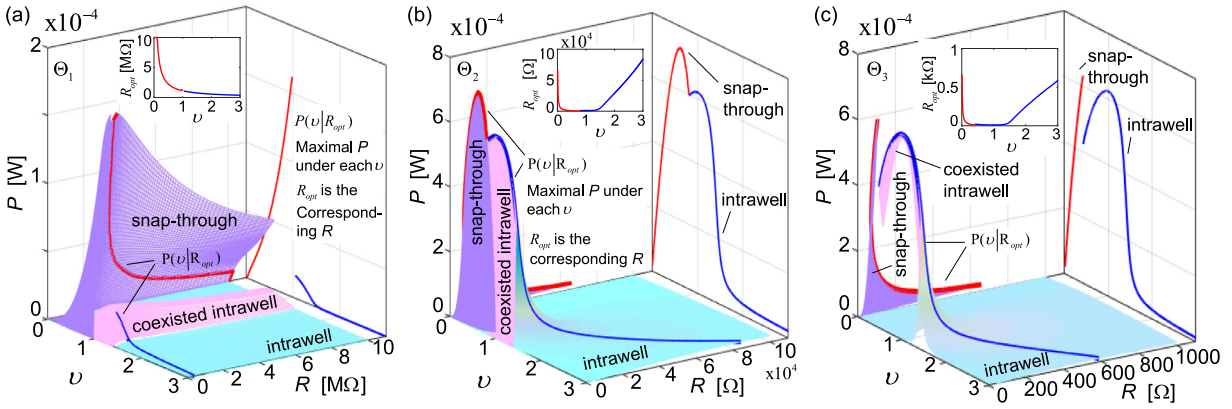

Fig. 12. Harvested power with respect to the excitation frequency and load resistance, and the adopted coupling constants are (a) $\Theta_1 = 3.27 \times 10^{-5}$N/V; (b) $\Theta_2 = 3.27 \times 10^{-3}$N/V; and (c) $\Theta_3 = 3.27 \times 10^{-2}$N/V. The insert is the optimal load resistance under each excitation frequency, and the projected curve $P(\upsilon|R_{opt})$ is the maximal harvested power with optimal load resistance adopted with respect to the excitation frequency.

load resistance that could induce snap-through vibration; while in the high excitation frequency range that only activates intrawell vibrations, the harvested power first increases up to its maximum and then gradually decreases with the increase of load resistance, as shown in Fig. 9(c).

The optimal load resistance corresponding to the maximal harvested power under fixed excitation level depends on the excitation frequency. Two illustrations are given with the excitation frequencies $\upsilon = 0.52$ and$\upsilon = 1.05$, respectively. The system performances are examined with successively varying load resistances with the other parameters the same as those adopted in Fig. 9, and are displayed in Figs. 11(a) and (b), respectively. It is found that the coexistence of snap-through and intrawell vibrations occurs in a range of moderate load resistances, beyond which only intrawell vibration occurs. Also, Fig. 11 reveals that the load resistance governs the harvested power induced from snap-through and intrawell vibrations in a linear fashion according to logarithmic changes of their values, which is similar to that in the linear energy harvester [61]. In each vibration branch, there exists a local optimal load resistance, including R^*_{snap}, $R^{*1}_{\text{intra}}$and R^{*2}_{intra}, which corresponds to the local maximal harvested power. The optimal load resistance R^*_{snap} that induces the maximal harvested power turns to be smaller for higher excitation frequency due to that the frequency range activating snap-through vibrations is reduced under higher load resistance in Fig. 9.

Moreover, Fig. 12 shows the harvested power with respect to the excitation frequency and load resistance, in which the insert is the optimal load resistance under each excitation frequency, and the projected curve is the maximal harvestable energy under each excitation frequency with the optimal load resistance adopted. For fixed coupling constant, the maximal harvestable power is achieved from snap-through vibration in moderate excitation frequency; while from intrawell vibration in high excitation frequency. With increment of the coupling constant, the maximal harvestable power $P(\upsilon|R_{opt})$ first increases and then decreases. Additionally, the optimal load resistance is excitation frequency dependent. On a wide range of excitation frequency, the optimal load resistance varies in a wide range when the coupling constant is low, while varies in a lower, more narrow range for higher coupling constant.

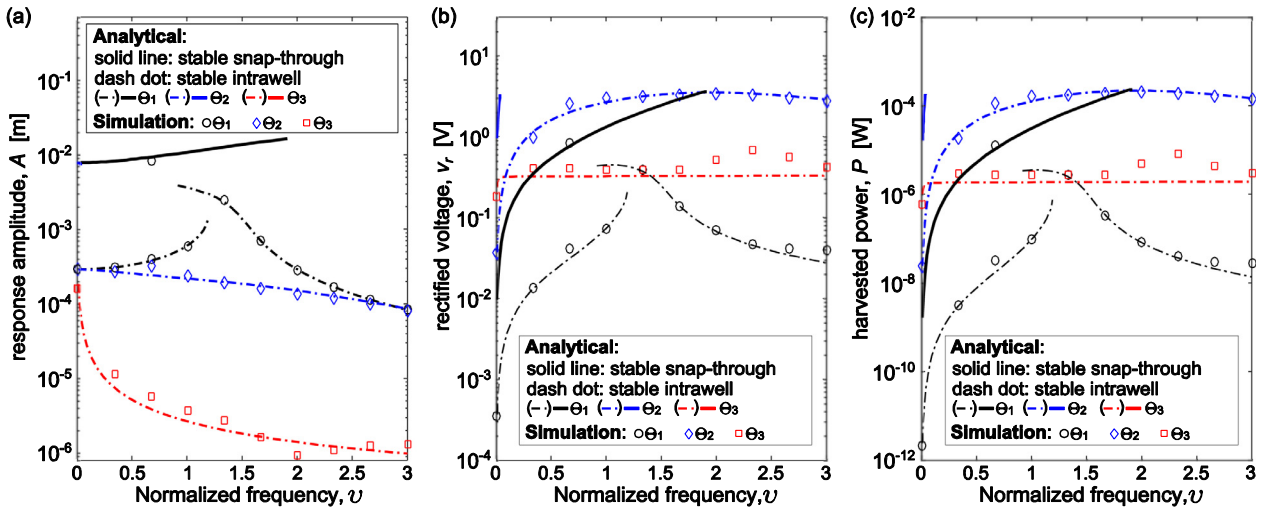

Fig. 13. Influence of coupling constants on (a) dynamic response, (b) rectified voltage and (c) harvested power. The excitation level is $p = 7\text{m/s}^2$ and the coupling constants are set to be $\Theta_1 = 3.27 \times 10^{-5}\text{N/V}$; $\Theta_2 = 3.27 \times 10^{-3}\text{N/V}$ and $\Theta_3 = 3.27 \times 10^{-2}\text{N/V}$.

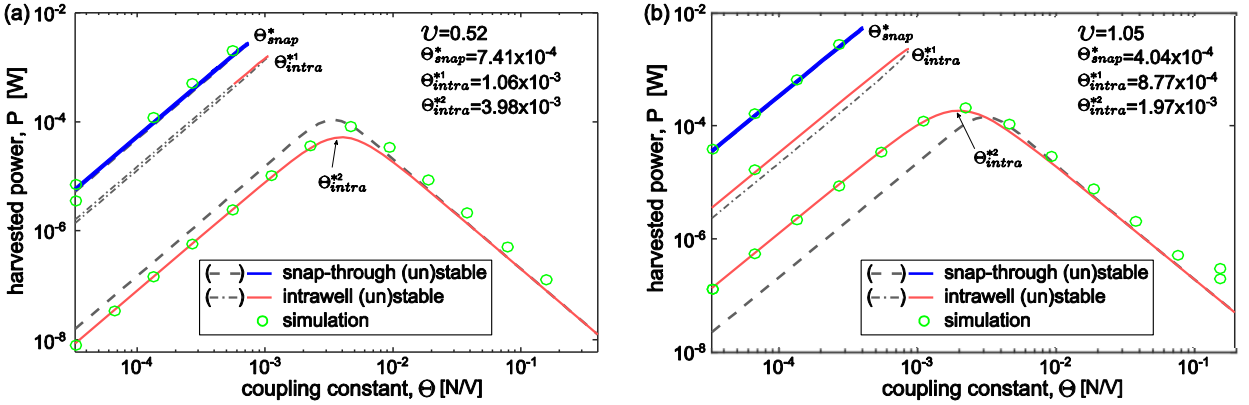

Fig. 14. Coupling constant dependence of the harvested power under the excitation level of $p = 7\text{m/s}^2$, and frequencies of (a) $\upsilon = 0.52$ and (b) $\upsilon = 1.05$.

5.3. Effect of coupling constant

To investigate the influence of the coupling constant on the system performance, three different-magnitude piezoelectric coupling constants of$\Theta_1 = 3.27 \times 10^{-5}\text{N/V}$, $\Theta_2 = 3.27 \times 10^{-3}\text{N/V}$ and $\Theta_3 = 3.27 \times 10^{-2}\text{N/V}$ are adopted to examine the corresponding dynamic response, rectified voltage and harvested power under a wide range of excitation frequencies $0 < \upsilon \leq 3$. The excitation level and load resistance are chosen as $p = 7\text{m/s}^2$ and $R = 56\text{k}\Omega$, respectively. Both analytically predicted stable responses and their numerical counterparts are shown in Fig. 13. Like the influence of load resistance in Fig. 9(a), greater coupling constant compromises the beneficial bandwidth of snap-through vibrations. The rectified voltage and harvested power are determined by both the mechanical vibration energy of the oscillator and the coupling constant. Higher coupling constant results in a larger proportion of mechanical energy transferred to electrical power, while also reduces the response amplitudes of each vibration branch which means less mechanical energy is captured by the oscillator. These two effects counterbalance each other, such that in the range of moderate coupling constants, larger constant like Θ_2 will extract higher rectified voltage and electrical power than smaller constant like Θ_1; while relatively large coupling constant like $\Theta_3$will result in much lower vibration amplitude, rectified voltage and harvested power, as shown in Fig. 13(b) and (c).

To illustrate the influence of successively varying coupling constant on harvested power and determine the optimal coupling constant under fixed excitation frequencies, two examples are examined when the system is excited at frequency of $\Omega = 0.52$ and$\Omega = 1.05$, respectively. The harvested power on successively varying coupling constants are derived and shown in Fig. 14. It reveals that the coexistence of snap-through and intrawell vibrations only occurs in a range of moderate coupling constants, beyond which only intrawell vibration exists. Also, it reveals that the coupling constant governs the harvested power from both snap-through and intrawell vibrations in a log-linear fashion. Considering the two-edged effects of the coupling constant on the harvester performance, it is predicted and shown in Fig. 14 that each vibration branch exists

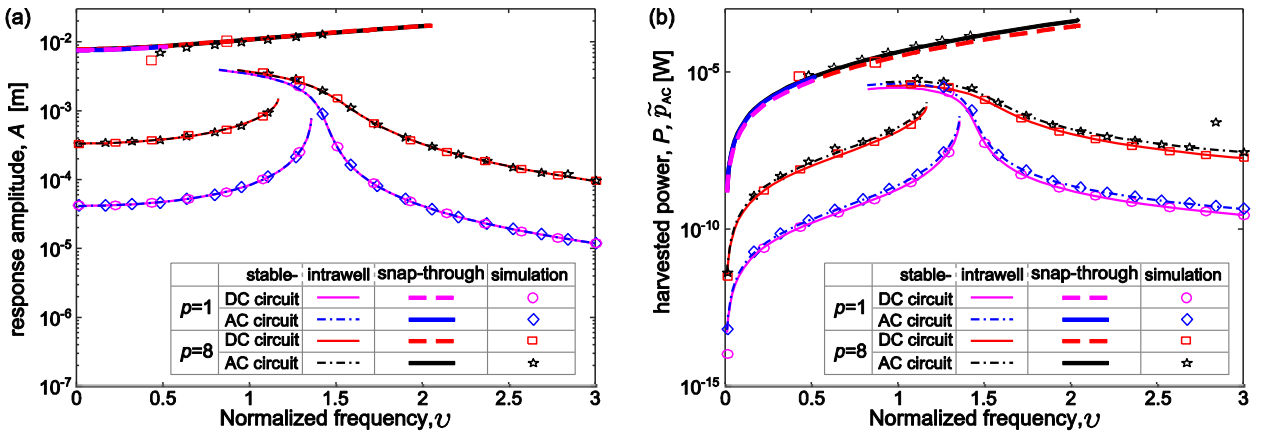

Fig. 15. Role comparison of DC interface and AC interface on (a) dynamic response and (b) harvested power. The excitation levels are $p = 1\text{m/s}^2$ and $p = 8\text{m/s}^2$, respectively.

an optimal coupling constant, Θ^*_{snap}, $\Theta^{*1}_{\text{intra}}$ and $\Theta^{*2}_{\text{intra}}$, which corresponds to the local maximal harvested power. Moreover, in moderate excitation frequency range that may activate snap-through vibrations with proper coupling constant, the optimal coupling constant Θ^*_{snap} which induces the highest electrical power turns to be smaller for higher excitation frequency because the effective frequency range that activates snap-through vibrations is shorter for higher coupling constant.

5.4. Comparison of AC and DC circuit influences on the harvester responses

The different roles of the AC circuit interface and the nonlinear, standard rectifying electrical circuit interface in the harvester systems are qualitatively and quantitively compared in this section. The AC circuit, implemented using a pure resistive load in majority of existing studies, mainly exhibits damping effect due to that the resistive load totally dissipates the converted electrical power. And this is also embodied in the analysis method [16] in which the piezovoltage is assessed to be proportional to the velocity. While for the standard rectifying electrical circuit, the converted electrical power is partially transferred back into mechanical energy during the blocked interval of the diode bridge, resulting in both equivalent damping and stiffness effects to the harvester system. This could also be embodied from Eq. (10) in which the piezovoltage mathematically contains both the damping term $\sin\omega t$(related with $\dot{x}$) and stiffness term $\cos\omega t$ (related with x).

To quantitively compare the roles of these two electrical circuit interfaces, the one-term harmonic balance method [16] is used to characterize the performance of AC circuit interfaced system. And for a fair and meaningful comparison with the DC voltage and harvested power of the standard rectifying electrical circuit, the effective value of the AC voltage, $\tilde{v}_{AC}$ and averaged harvested power, $\tilde{P}_{AC}$ across the load resistance in the AC circuit are adopted and expressed as

$$\tilde{v}_{AC} = \frac{1}{\sqrt{2}} \cdot \frac{A\Theta\omega}{\sqrt{C_p^2\omega^2 + 1/R^2}}. \tag{24}$$

$$\tilde{P}_{AC} = \frac{\tilde{v}_{AC}^2}{R} = \frac{A^2\Theta^2\omega^2 R}{2\left(C_p^2\omega^2R^2 + 1\right)}. \tag{25}$$

A comparison is conducted between bistable harvesters interfaced with the AC circuit and the standard rectifying electrical circuit, adopting a mild coupling constant of $\Theta = 3.27 \times 10^{-5}\text{N/V}$ and load resistance of $R = 56\text{k}\Omega$. The other system parameters are the same as those in Table 1. The system dynamic responses and harvested powers (P in Eq. (21) for DC power and $\tilde{P}_{AC}$ in Eq. (25) for AC power) under harmonic excitation levels of $p = 1\text{m/s}^2$ and $p = 8\text{m/s}^2$ are shown in Fig. 15. Fig. 15(a) reveals that the vibration amplitudes of these two systems are almost the same, thus the same amount of vibration energy is provided for these two circuits. In Fig. 15(b), both analytical and numerical results show that the harvested power in the standard rectifying electrical circuit is close to but less than the averaged power in the AC circuit in the whole excitation frequency range, which is resulted from the phenomenon that some converted electrical power in the standard rectifying electrical circuit is transferred back to mechanical energy while all the converted electrical power flowing into the AC circuit is consumed by the resistive load.

Further comparisons between these two circuit interfaces are conducted for a wide range of piezoelectric coupling constants. In the analysis, a moderate load resistance is adopted, $R = 56\text{k}\Omega$. The steady state dynamic responses and harvested power under the excitation level of $p = 8\text{m/s}^2$ and frequency of $\upsilon = 0.55$ are estimated analytically and numerically, as shown in Fig. 16. It reveals that snap-through vibrations can be activated with moderate coupling constants (below the optimal coupling constant Θ^*_{snap}) for these two circuit interfaced systems while the range of the standard rectifying electrical circuit is a little wider than that of AC circuits. To explicitly illustrate the different effects of the AC and DC circuits,

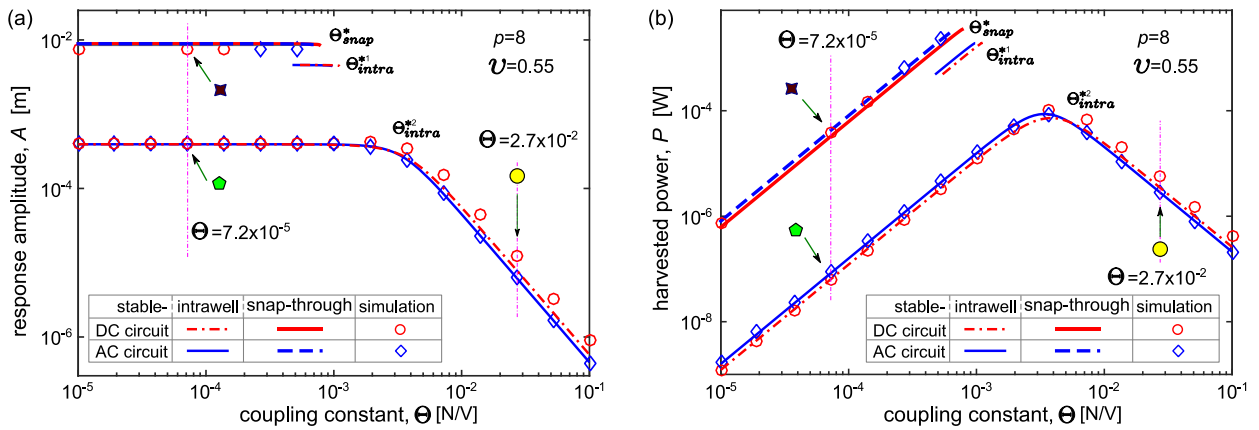

Fig. 16. Comparison of standard rectifying electrical and AC circuits interfaced systems with respect to coupling constants on (a) Response amplitude and (b) harvested power. The time-varying waveforms under the condition that marked using symbols are displayed in Figs. (17) and (18).

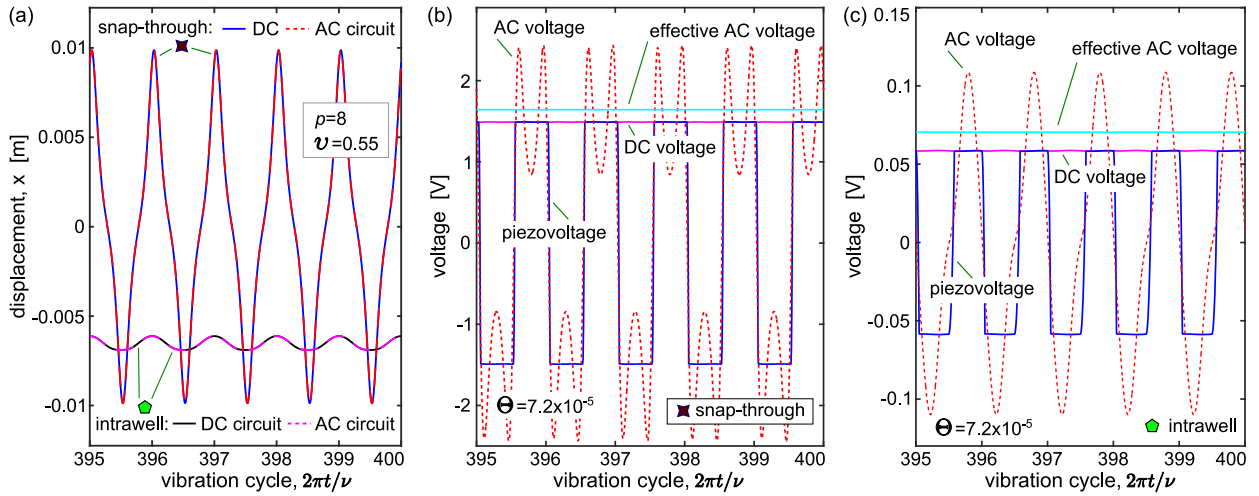

Fig. 17. Time-varying waveforms comparison of the dynamic responses and voltage generated by harvester interfaced with AC and DC circuits under moderate coupling constant.

the waveforms of the dynamic responses and induced voltages under two specific coupling constants that are marked with symbols in Fig. 16 are numerically simulated and displayed in Figs. (17) and (18), respectively. Thus, for moderate coupling constants which are less than $\Theta^{*2}_{\text{intra}}$ in Fig. 16, the vibration amplitudes from these two circuit interfaced systems are almost the same, and thus the AC circuit extracts more electrical power in this range. However, for relatively high coupling constants such as those higher than $\Theta^{*2}_{\text{intra}}$ in Fig. 16 where vibration amplitude is more significantly affected, both analytical and numerical results show that the dynamic response amplitudes of the standard rectifying electrical circuit are clearly higher than those of the AC circuit, and accordingly the standard rectifying electrical circuit harvests more electrical power than the AC circuit.

In addition, the performance of these two electrical circuits are compared for a wide range of load resistances. The piezoelectric coupling constant of $\Theta = 3.27 \times 10^{-3}$N/V is adopted while other system parameters are the same as those in Table 1. The steady state dynamic responses and harvested power of these two circuit-interfaced systems under the excitation level of $p = 8\text{m/s}^2$ and frequency of $\upsilon = 0.55$ are plotted in Fig. 19, respectively. It shows that under this excitation condition these two systems can activate snap-through vibrations in the range of moderate load resistances (less than R^{*}_{snap}) while the range for the standard rectifying electrical circuit is a little wider than that for the AC circuit. Also, for moderate load resistances less than R^{*2}_{intra} in Fig. 19, the vibration amplitudes of these two systems are almost the same, and thus the AC circuit extracts higher electrical power. However, for relatively high load resistances (higher than R^{*2}_{intra} in Fig. 19) where the dynamic responses are significantly reduced by the circuits, both analytical and numerical results show that the vibration amplitudes from the standard rectifying electrical circuit system are higher than those from the AC circuit system, and the standard rectifying electrical circuit accordingly extracts more electric power than the AC circuit.

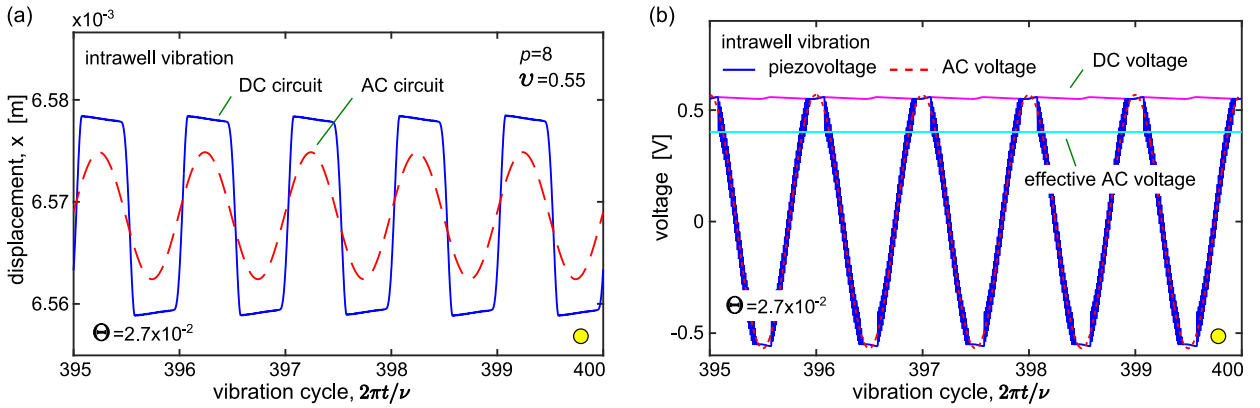

Fig. 18. Time-varying waveforms comparison of the dynamic responses and voltage generated by harvester interfaced with AC and DC circuits under relatively large coupling constant.

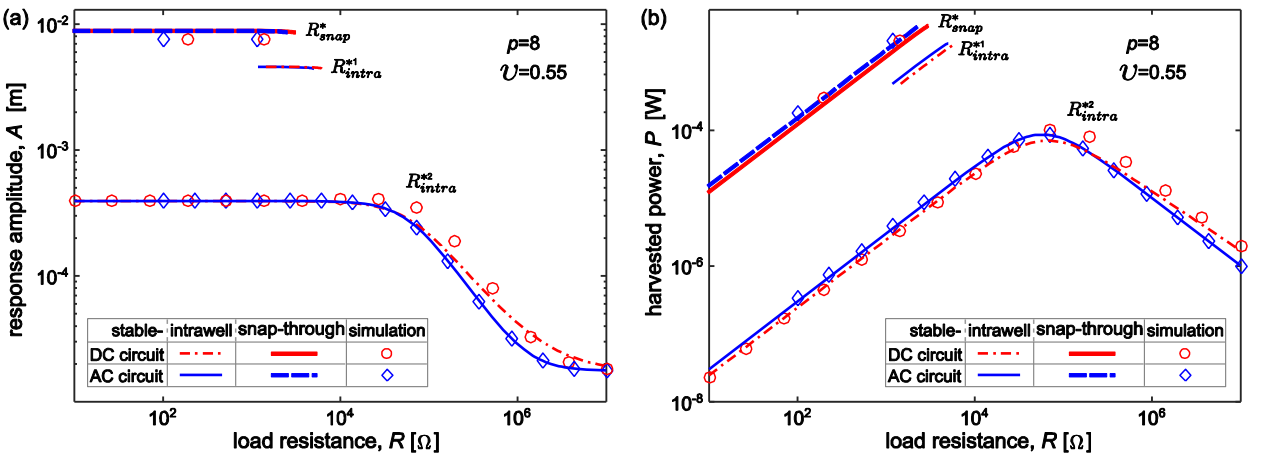

Fig. 19. Performance comparison of standard rectifying electrical and AC circuits interfaced systems with respect to increasing load resistances. (a) Dynamic response amplitude and (b) harvested power.

6. Experiment investigation

To validate the analytically and numerically characterized performances of bistable harvesters interfaced with the standard rectifying electrical circuit, a series of experiments are conducted using the system described in Section 4. The base excitation is harmonic, of which the acceleration amplitude and frequency are accurately controlled using National Instruments outputs channel through a LABVIEW software interface. The frequency dependence of harvested power is tested under three different excitation levels [56], with the evaluated effective acceleration amplitudes 3.14 m/s^2, 3.81 m/s^2 and 4.34 m/s^2. Under each excitation level, three individual frequency sweeping tests are conducted (frequency increasing once, decreasing twice with the initial state in each intra well, respectively), such that the multiple vibrations of bistable oscillator are captured. The sweeping frequency is in the range of $f = \omega/2\pi = [3,\ 30\text{Hz}]$ with the variation interval of 1 Hz. The base motion for each excitation level and frequency is set to last for 120 s before changing the excitation frequency, ensuring that the charging system reaches steady state. After the data are recorded, the rectified voltage v_r under each excitation frequency is calculated as the sum of the mean value of the voltage across the load resistance during the last ten base motion cycles and the voltage drop across the diodes. The harvested power is further calculated by $P = v_r^2/R$. The rectified voltages and harvested powers are shown in Fig. 20 in which the horizontal axis represents the base excitation frequency and the vertical axis data indicates the mean measurement at each given excitation frequency. The left column shows the rectified voltage induced by both snap-through and intrawell oscillations, and the right column displays the corresponding harvested power. As base excitation level increases, top to bottom in Fig. 20, the frequency range of the snap-through oscillation gradually increases, and the rectified voltage and harvested power also increase due to the increase of input energy.

Comparing the analytical predictions with experimental measurements, it reveals that they are overall in good agreement in both snap-through and intrawell vibration regimes. While local deviations between analytical and experimental results are observed in the intrawell branch near the excitation frequency of 12 Hz under three excitation levels. The

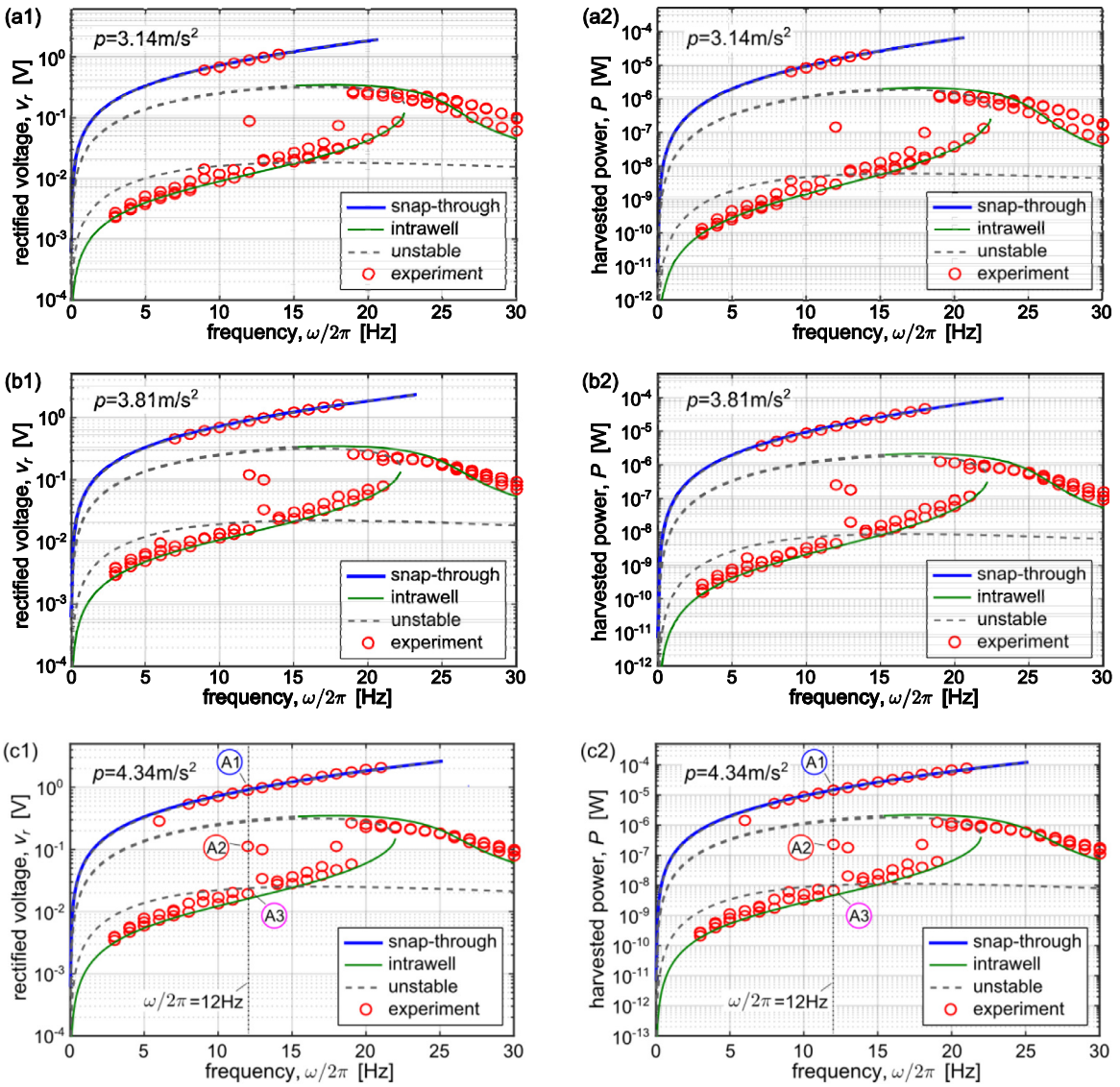

Fig. 20. Experimentally measured bistable harvester responses when connected to a standard rectifying electrical circuit. Left column (1), rectified voltage across the load resistance at different excitation frequencies. Right column (2), harvested power at different excitation frequencies. Effective base acceleration amplitude of (a) $p = 3.14\text{m/s}^2$, (b) $p = 3.81\text{m/s}^2$ and (c) $p = 4.34\text{m/s}^2$.

experimentally measured trajectories of the motions as labeled by A1, A2, and A3 in Fig. 20(c) are displayed in Fig. 21, in which the dashed curves are the analytical results. For the motions in Fig. 21(a) and (c) in which the fundamental frequency is the primary component in the frequency spectrum, the analytical prediction basically coincides with the experiment measurement. Considering the natural frequency of the linearized intrawell vibration could be estimated as $\sqrt{2k_1/m}/2\pi$ =24.74Hz, it is experimentally found from Fig. 21(b) that super harmonic resonance occurs in the vibration near 12 Hz and thus the super harmonic components become significant in this case. Despite this trade-off in predictive ability, the analytical estimations of harvested power are still close to the actual values under most excitation frequencies that are suitable for engineering applications.

To validate the influence of load resistance on the energy harvesting performance, experiments are further conducted using the same bistable energy harvesting system with varying load resistance. The base excitation level and frequency are fixed at $3.32\,\text{m/s}^2$ and 10 Hz, respectively. A series of load resistances from 1kΩ up to 10MΩare individually connected in the standard rectifying electrical circuit. Fig. 20 reveals that the adopted excitation level and frequency are able to activate both snap-through and intrawell oscillations. For each connected load resistance, three different vibration responses of the bistable beam, i.e., snap-through and intrawell vibration in each well, are activated and each vibration lasts till the measured rectified voltage no longer varies. Considering only the input voltage within the range of [−10 V, 10 V] can be

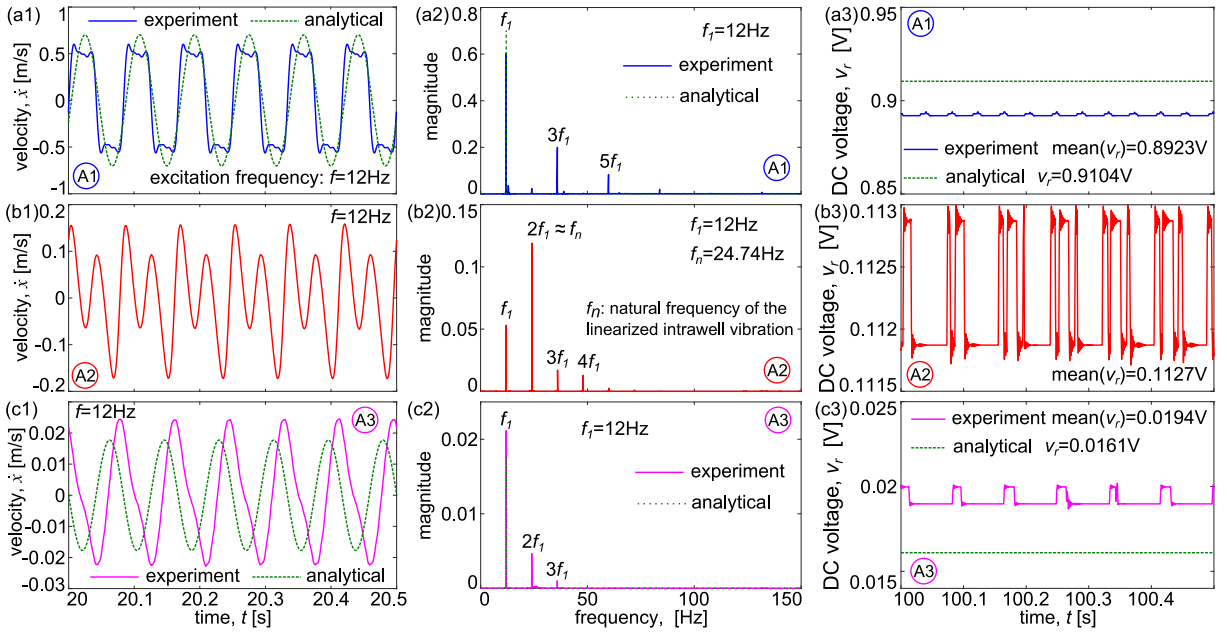

Fig. 21. Experimentally measured (a) relative velocity of the beam with respect to the base; (b) frequency spectrum of relative velocity; and (c) rectified voltage. The up-to-low rows correspond to the motions as indicated by the labels A1, A2, and A3 in Fig. 20(c).

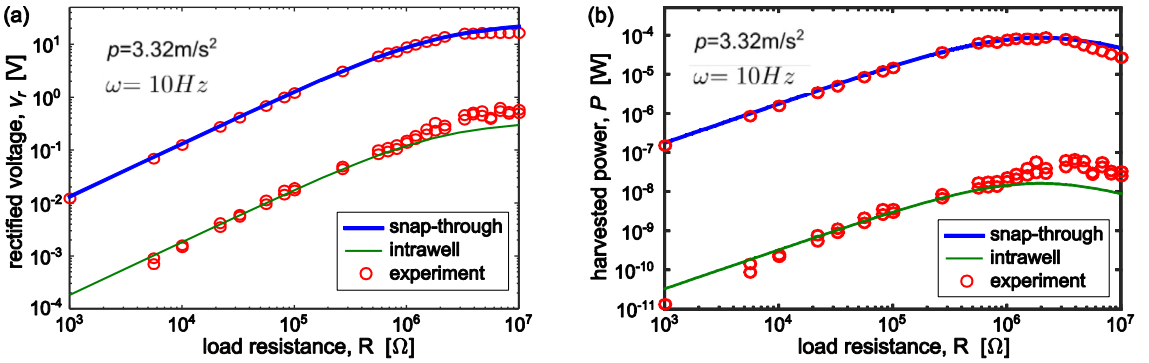

Fig. 22. Load resistance dependence of (a) rectified voltage and (b) average harvested power for excitation level and frequency of $p = 3.32\text{m/s}^2$ and $\omega = 10$Hz, respectively.

recognized by the NI data acquisition system, higher rectified voltage overreaching the boundary is measured using a multimeter. The red circles in Fig. 22 show the measured rectified voltages and corresponding harvested powers under different load resistances. It reveals that the energy harvesting performance is load resistance dependent. The rectified voltage induced from snap-through oscillation increases rapidly with the increase of load resistance before reaching 3.3MΩ, and it then reaches its maximum and remains near constant when the load resistance exceeds 3.3MΩ. Accordingly, the harvested power first increases and then drops down for relatively high load resistances and the optimal load resistance corresponding to the highest power occurs at 2MΩ. The analytical predictions are also displayed in Fig. 22. It reveals that the analytical predictions and experimental measurements are in good agreement. Moreover, the analytical prediction of the optimal load resistance is accurately validated via the experiment measurements.

7. Conclusion

To predict the electrical energy storage performance and reveal the DC circuit effects of harmonically excited bistable energy harvester interfaced with a standard rectifying electrical circuit, an analytical method is proposed in this research. During the route of the analysis method, a key, prior processing that reveals the relation of the piecewise piezovoltage and smooth dynamic responses based on the energy equivalence is utilized which enables the followed harmonic balance analysis. Via predicting the system performance under different excitations and system parameters, and accompany with numerical simulation validations, it shows that the approach provides an effective tool to identify the influence of harmonic

excitation and system design parameters on the dynamic responses and the harvested power. Parameter studies reveal that higher coupling constant or load resistance will compromise the beneficial bandwidth of snap-through vibration. In the range of moderate coupling constants and load resistances, higher rectified voltage and harvested power are achieved via larger coupling constant or load resistance. While in the range of relatively large coupling constants and load resistances, larger coupling constant or load resistance will lead to less harvested power. Also, the optimal load resistance and coupling constant are excitation frequency dependent. Under a wide range of excitation frequencies, the optimal load resistance varies in a wide range when the coupling constant is low, while varies in a lower, very narrow range when the coupling constant is large. Comparisons of the roles of the AC circuit and standard rectifying circuit are also conducted. It is concluded that the AC circuit exhibits equivalent damping effect while the standard rectifying electrical circuit exhibits both equivalent damping and stiffness effects to the harvester system. These different effects explain the phenomena that for moderate coupling constant and load resistance, more electric power is extracted via the AC circuit; while for relatively high coupling constant or load resistance, the standard rectifying electrical circuit will possess larger vibration amplitude and thus more electric power than the AC circuit. In this study, it is illustrated that while only considering the fundamental harmonic component of the nonlinear dynamic response, the proposed analytical method provides good predictions as compared to the numerical and experiential results. On the other hand, to obtain even higher accuracy, the higher harmonic components should be considered in future investigations. Potentially, the proposed analysis frame in this paper could also be applied for analyzing the steady state dynamic responses and harvested power of bistable energy harvesters interfaced with more complex nonlinear energy harvesting interfaces such as aforementioned PSSHI and SECE circuits.

Acknowledgements

Useful discussions with Dr. Hongbin Fang (at Fudan University, Shanghai, China) are gratefully acknowledged. This work is supported in part by the Fundamental Research Funds for the Central Universities Grant 31020191A009, China Postdoctoral Science Foundation grant 2018M631196, the University of Michigan Collegiate Professorship, The Ohio State University Center for Automotive Research, and the U.S. National Science Foundation grants 1661572 and 1661568.

References

[1] Ujihara M, Carman G, Lee D. Thermal energy harvesting device using ferromagnetic materials. Appl Phys Lett 2007;91:093508.
[2] Smith JG, Faucheaux JA, Jain PK. Plasmon resonances for solar energy harvesting: a mechanistic outlook. Nano Today 2015;10:67–80.
[3] Bowers BJ, Arnold DP. Spherical, rolling magnet generators for passive energy harvesting from human motion. J Micromech Microeng 2009;19:094008.
[4] Hosseinloo AH, Turitsyn K. Non-resonant energy harvesting via an adaptive bistable potential. Smart Mater Struct 2016;25:015010.
[5] Tang J, Wang K. Active-passive hybrid piezoelectric networks for vibration control: comparisons and improvement. Smart Mater Struct 2001;10(4):794–806.
[6] Wang K, Tang J. Adaptive structural systems with piezoelectric transducer circuitry. New York: Springer; 2008.
[7] Zhou S, Zuo L. Nonlinear dynamic analysis of asymmetric tristable energy harvesters for enhanced energy harvesting. Commun Nonlinear Sci Numer Simul 2018;61:271–84.
[8] Sodano HA, Inman DJ, Park G. Comparison of piezoelectric energy harvesting devices for recharging batteries. J Intell Mater Syst Struct 2005;16:799–807.
[9] Harne R, Wang K. A review of the recent research on vibration energy harvesting via bistable systems. Smart Mater Struct 2013;22:023001.
[10] Sodano HA, Inman DJ, Park G. A review of power harvesting from vibration using piezoelectric materials. Shock Vibr Digest 2004;36(3):197–205.
[11] Priya S, Inman DJ. Energy harvesting technologies. New York: Springer; 2009.
[12] Yuan T, Yang J, Chen L. Nonlinear dynamics of a circular piezoelectric plate for vibratory energy harvesting. Commun Nonlinear Sci Numer Simul 2018;59:651–6.
[13] Hu Y, Xue H, Hu H. A piezoelectric power harvester with adjustable frequency through axial preloads. Smart Mater Struct 2007;16:1961–6.
[14] Abdelkefi A, Najar F, Nayfeh A, Ayed S. An energy harvester using piezoelectric cantilever beams undergoing coupled bending-torsion vibrations. Smart Mater Struct 2011;20:115007.
[15] Erturk A, Inman D. Broadband piezoelectric power generation on high-energy orbits of the bistable duffing oscillator with electromechanical coupling. J Sound Vib 2011;330(10):2339–53.
[16] Harne R, Thota M, Wang K. Concise and high-fidelity predictive criteria for maximizing performance and robustness of bistable energy harvesters. Appl Phys Lett 2013;102:053903.
[17] Harne R, Wang K. Harnessing bistable structural dynamics: for vibration control, energy harvesting, and sensing. John Wiley and Sons; 2017.
[18] Cottone F, Gammaitoni L, Vocca H, Ferrari M, Ferrari V. Piezoelectric buckled beams for random vibration energy harvesting. Smart Mater Struct 2012;21:035021.
[19] Formosa F, Bussing T, Badel A, Marteau S. Energy harvesting device with enlarged frequency bandwidth based on stochastic resonance. Proc Power-MEMS 2009:229–32.
[20] Jung S-M, Yun K-S. A wideband energy harvesting device using snap-through buckling for mechanical frequency-up conversion. Micro electro mechanical systems (MEMS), 2010 IEEE 23rd international conference on Wanchai , Hong Kong; 2010.
[21] Liu Y, Guo P, Zhang C. Transient dynamics and electric power estimation of bistable energy harvesters under impulsive excitations. IEEE Access 2019;7:36233–45.
[22] Ando B, Baglio S, Latorre L, Maiorca F, Nouet P, Trigona C. Magnetically-coupled cantilevers with antiphase bistable behavior for kinetic energy harveting. Procedia Eng 2012;47:1065–8.
[23] Daqaq MF, Masana R, Erturk A, Quinn DD. On the role of nonlinearities in vibration energy harvesting: a critical review and discussion. Appl Mech Rev 2014;66:040801.
[24] Ferrari M, Ferrari V, Guizzetti M, Ando B, Baglio S, Trigona C. Improved energy harvesting from wideband vibrations by nonlinear piezoelectric converters. Sens Actuat A 2010;162:425–31.
[25] Erturk A, Hoffmann J, Inman D. A piezomagnetoelastic structure for broadband vibration energy harvesting. Appl Phys Lett 2009;94:254102.
[26] Harne R, Wang K. On the fundamental and superharmonic effects in bistable energy harvesting. J Int Mater Syst Struct 2013;25:937–50.
[27] Arrieta A, Hagedorm P, Erturk A, Inman D. A piezoelectric bistable plate for nonlinear broadband energy harvesting. Appl Phys Lett 2010;97:104102.
[28] Pellegrini SP, Tolou N, Schenk M, Herder JL. Bistable vibration energy harvesters: a review. J Intell Mater Syst Struct 2012;24(11):1303–12.
[29] Zhang C, Harne RL, Li B, Wang K. Statistical quantification of DC power generated by bistable piezoelectric energy harvesters when driven by random excitations. J Sound Vib 2019;442:770–86.

[30] Zhang C, Harne R, Li B, Wang K. Reconstructing the transient, dissipative dynamics of a bistable duffing oscillator with an enhanced averaging method and Jacobian elliptic functions. Int J Non Linear Mech 2016;79:26–37.
[31] Liu W, Formosa F, Badel A. Optimization study of a piezoelectric bistable generator with doubled voltage frequency using harmonic balance method. J Intell Mater Syst Struct 2016;28(5):671–86.
[32] Stanton SC, Owens BA, Mann BP. Harmonic balance analysis of the bistable piezoeletric inertial generator. J Sound Vib 2012;331:3617–27.
[33] Mann B, Owens B. Investigations of a nonlinear energy harvester with a bistable potential well. J Sound Vib 2010;329:1215–26.
[34] Shu Y, Lien I, Wu W. An improved analysis of the SSHI interface in piezoelectric energy harvesting. Smart Mater Struct 2007;16:2253–64.
[35] Lefeuvre E, Badel A, Richard C, Petit L, Guyomar D. A comparison between several vibration-powered piezoelectric generators for standalone systems. Sens Actuat A 2006;126:405–16.
[36] Kong N, Ha DS, Erturk A, Inman DJ. Resistive impedance matching circuit for piezoelectric energy harvesting. J Intell Mater Syst Struct 2010;21:1293–302.
[37] Ottman GK, Hofmann HF, Bhatt AC, Lesieutre GA. Adaptive piezoelectric energy harvesting circuit for wireless romote power supply. IEEE Trans Power Electron 2002;17:669–76.
[38] Shu Y, Lien I. Analysis of power output for piezoelectric energy harvesting systems. Smart Mater Struct 2006;15:1499–512.
[39] Liang J, Liao W-H. Impedance modeling and analysis for piezoelectric energy harvesting systems. IEEE/ASME Trans Mechatron 2012;17:1145–57.
[40] Guyomar D, Badel A, Lefeuvre E, Richard C. Toward energy harvesting using active materials and conversion improvement by nonlinear processing. IEEE Trans Ultrason Ferroelectr Freq Control 2005;52:584–95.
[41] Taylor GW, Burns JR, Kammann SM, Powers WB, Welsh TR. The energy harvesting EEL: a small subsurface ocean/river power generator. IEEE J Oceanic Eng 2001;26:539–47.
[42] Liang J, Liao W-H. Improved design and analysis of selt-powerd synchronized switch interface circuit for piezoelectric energy harvesting systems. IEEE Trans Ind Electron 2012;59:1950–60.
[43] Hsieh P-H, Chen C-H, Chen H-C. Improving the scavenged power of nonlinear piezoelectric energy harvesting interface at off-resonance by introducing switching delay. IEEE Trans Power Electron 2015;30:3142–55.
[44] Lefeuvre E, Badel A, Richard C, Guyomar D. Energy harvesting sing piezoelectric materials: case of random vibrations. J Electroceram 2007;19:349–55.
[45] Tang L, Yang Y. Analysis of synchronized charge extraction for piezoelectric energy harvesting. Smart Mater Struct 2011;20:085022.
[46] Morel A, Pillonnet G, Gasnier P, Lefeuvre E, Badel A. Frequency tuning of piezoelectric energy harvesters thanks to a short-circuit synchronous electric charge extraction. Smart Mater Struct 2019;28:025009.
[47] Cai Y, Manoli Y. System design of a time-controlled broadband piezoelectric energy harvesting interface circuit. *IEEE international symposium on circuits and systems (ISCAS)*, Lisbon, Portugal, May 24-27, 2015; 2015.
[48] Chen Y-Y, Vasic D, Liu Y-P, Costa F. Study of a piezoelectric switching circuit for energy harvesting with bistable broadband technique by work-cycle analysis. J Intell Mater Syst Struct 2013;24(2):180–93.
[49] Liu W, Badel A, Formosa F, Wu Y, Agbossou A. Wideband energy harvesting using a combination of an optimized synchronous electric charge extraction circuit and a bistable harvester. Smart Mater Struct 2013;22:125038.
[50] Singh KA, Kumar R, Weber RJ. A broadband bistable piezoelectric energy harvester with nonlinear high-power extraction. IEEE Trans Power Electron 2015;30(12):6763–74.
[51] Wu Y, Badel A, Formosa F, Liu W, Agbossou A. Nonlinear vibration energy harvesting device integrating mechanical stoppers used as synchronous mechanical switches. J Intell Mater Syst Struct 2014;25:1658–63.
[52] Cheng C, Chen Z, Xiong Y, Shi H, Yang Y. A high-efficiency, self-powered nonlinear interface circuit for bi-stable rotating piezoelectric vibration energy harvesting with nonlinear magnetic force. Int J Appl Electromag Mech 2016;51:235–48.
[53] Dai Q, Harne RL. Investigation of direct current power delivery from nonlinear vibration energy harvesters under combined harmonic and stochastic excitations. J Intell Mater Syst Struct 2018;29(4):514–29.
[54] Lan C, Tang L, Harne RL. Comparative methods to assess harmonic response of nonlinear piezoelectric energy harvesters interfaced with AC and DC circuits. J Sound Vib 2018;421:61–78.
[55] Harne R, Zhang C, Li B, Wang K. An analytical approach for predicting the energy capture and conversion by impulsively-excited bistable vibration energy harvesters. J Sound Vib 2016;373:205–22.
[56] Erturk A, Inman D. Issues in mathematical modeling of piezoelectric energy harvesters. Smart Mater Struct 2008;17(6):065016.
[57] Harne RL, Dai Q. Characterizing the robustness and susceptibility of steady-state dynamics in post-buckled structures to stochastic perturbations. J Sound Vib 2017;395:258–71.
[58] Kasyap A. Development of mems-based piezoelectric cantilever arrays for vibration energy harvesting. University of Florida; 2006.
[59] Rao SS, Yap FF. Mechanical vibration. forth ed. Addison-Wesley; 1995.
[60] Mann BP, Barton DA, Owens BA. Uncertainty in performance for linear and nonlinear energy harvesting strategies. J Intell Mater Syst Struct 2012;23(13):1451–60.
[61] Erturk A, Inman DJ. An experimentally validated bimorph cantilever model for piezoelectric energy harvesting from base excitations. Smart Mater Struct 2009;18:025009.